Available online at www.sciencedirect.com
ScienceDirect
Intermetallics 15 (2007) 1612–1622
Intermetallics
www.elsevier.com/locate/intermet

Shape-memory NiTi foams produced by solid-state replication with NaF

Ampika Bansiddhi, David C. Dunand*

Department of Materials Science and Engineering, Northwestern University, Evanston, IL 60208, USA

Received 24 April 2007; accepted 28 June 2007
Available online 30 August 2007

Abstract

A martensitic NiTi foam was produced by hot isostatic pressing a blend of NiTi and NaF powders and subsequent dissolution of the NaF phase. The NiTi foam consists of 40 vol.% near-fully open pores, 240 μm in size, and with ragged surfaces due to incomplete NiTi powder densification. Near linear stress–strain curves are measured in compression with an average loading stiffness of 4 GPa, well below the unloading stiffness of 13 GPa because of detwinning on loading. Shape-memory recovery after unloading corresponds to 85–89% of the unloading plastic strain. After sintering at 1250 °C, the foam exhibits 20% porosity, smaller, smoother and partially-closed pores, and a shift in composition towards a martensite/austenite mixture at ambient temperature. This new composition allows for the activation of the superelastic effect in the austenite during loading and unloading resulting in average stiffnesses of 6–12 GPa, and the shape-memory effect in the martensite with 60–97% of the plastic strain recoverable.

Keywords: A. Intermetallics, miscellaneous; B. Shape-memory effects; C. Hot isostatic pressing

1. Introduction

The near-equiatomic NiTi ordered intermetallic exhibits shape-memory or superelastic properties, depending on phases present, which provide high recoverable strains, good mechanical damping and large energy absorption [1]. NiTi foams can utilize the combined attributes of the NiTi material (e.g., shape-memory or superelasticity, high yield strength and ductility, good corrosion resistance and biocompatibility) and the foam architecture (e.g., low density and stiffness, high energy absorption and surface area). NiTi foams may thus find multi-functional applications such as bone implants [2–5], impedance-matching connectors between structural parts [6], energy-absorbing structures [7,8], separators [9] and actuators [10].

Foaming NiTi through the liquid route is very challenging, due to its high melting point (1310 °C), its extreme chemical reactivity with crucibles and atmospheric gases, and the need to tightly control composition to achieve shape-memory or superelastic properties. Therefore, to date, powder-metallurgy techniques have been exclusively used to fabricate porous NiTi (with the exception of Ref. [11] using zone melting in a hydrogen atmosphere). These solid-state methods use elemental or pre-alloyed powders and can be divided into five main groups: conventional sintering [12], reactive sintering [13–19], spark plasma sintering [20], self-propagating high-temperature synthesis (SHS) [21–27] and gas expansion in the solid-state after gas entrapment by hot isostatic pressing (HIP) [6,28].

None of these methods allows for an independent control of pore size and volume fraction, which are determinants for the thermo-mechanical properties of NiTi foams. In particular, sintering methods typically lead to relatively low porosities and small pores, dictated by the initial powder size; foam strength is often reduced due to incomplete sintering of the powders. SHS suffers from inhomogeneous pore size distribution as well as undesirable intermetallic phases [13,25,26]. Finally, the high creep strength and low creep ductility of NiTi prevent the achievement of high porosities in the gas expansion method [28].

* Corresponding author.
E-mail address: dunand@northwestern.edu (D.C. Dunand).

0966-9795/$ - see front matter © 2007 Elsevier Ltd. All rights reserved.
doi:10.1016/j.intermet.2007.06.013

Another processing method (used previously for Ti-, A1-, Ni-, Cu-, and Fe-based foams [29–36] but never, to our knowledge, for NiTi foams) is based on powder densification in the presence of a space-holder which is removed during or after the powder densification, resulting in a metallic foam with open porosity. Control of the pore volume fraction, shape and size are all accomplished by selection of the space-holder materials which have included in previous studies; sodium chloride [29] or carbamide [30,31] for aluminum foams, polymers [32] or potassium carbonate [33] for copper foams, sodium carbonate for nickel foams [34], and ammonium bicarbonate [35] or magnesium [36] for titanium foams.

To apply this solid-state replication method to the fabrication of NiTi foams, two issues must be addressed. First, the space-holder must be chemically unreactive with NiTi at the densification temperature. We choose here sodium fluoride (NaF) due to its thermodynamic stability in contact with nickel and titanium, its high melting point (993 °C) and its relatively high solubility in water (42.2 g/L at 18 °C [37]). Furthermore, NaF is a common, low-cost salt which can be easily recycled by precipitation after dissolution from the foam. The second issue pertains to the low diffusivity of NiTi resulting from its ordered crystal structure, which makes full densification of NiTi powders by pressureless sintering difficult to achieve. We address this issue by using HIP to enhance densification of the NiTi powders in the presence of NaF.

We present here the microstructure as well as physical and mechanical properties (including shape-memory properties) of an open porosity NiTi foam produced by the above solid-state replication method, using pre-alloyed NiTi powders and NaF powders as space-holder. We also examine the effect of a subsequent sintering step on this foam in terms of structure and properties, including the emergence of superelasticity.

2. Experimental procedures

2.1. Materials and processing

Pre-alloyed near-equiatomic NiTi powders with 99.9% purity and 44–177 μm particle size were used. These were the same powders (procured from Special Metals Corp., NY) used in previous study [38]. High-purity (99.995% pure) NaF powders were procured from Alfa Aesar, MA and sieved in the range of 62–250 μm. The typical morphologies of the NiTi and sieved NaF powders are illustrated in Fig. 1(a and b): NiTi powders are nearly spherical and have a smooth surface while the NaF powders have a blocky, equiaxed shape.

A mixture of 59.9 vol.% NiTi and 40.1 vol.% NaF powders was mechanically blended in a twin-shell dry blender for 40 min and poured into a mild steel can with 35 mm outer diameter and 1.6 mm wall thickness. The evacuated and sealed can was HIP-densified by UltraClad Corp. (MA) at 950 °C for 4 h under a pressure of 100 MPa. The HIP temperature was selected to be high enough to allow densification of the NiTi powders (950 °C corresponds to a homologous temperature of 0.77, given the NiTi melting point of 1310 °C) while remaining below the NaF space-holder melting point of 993 °C.

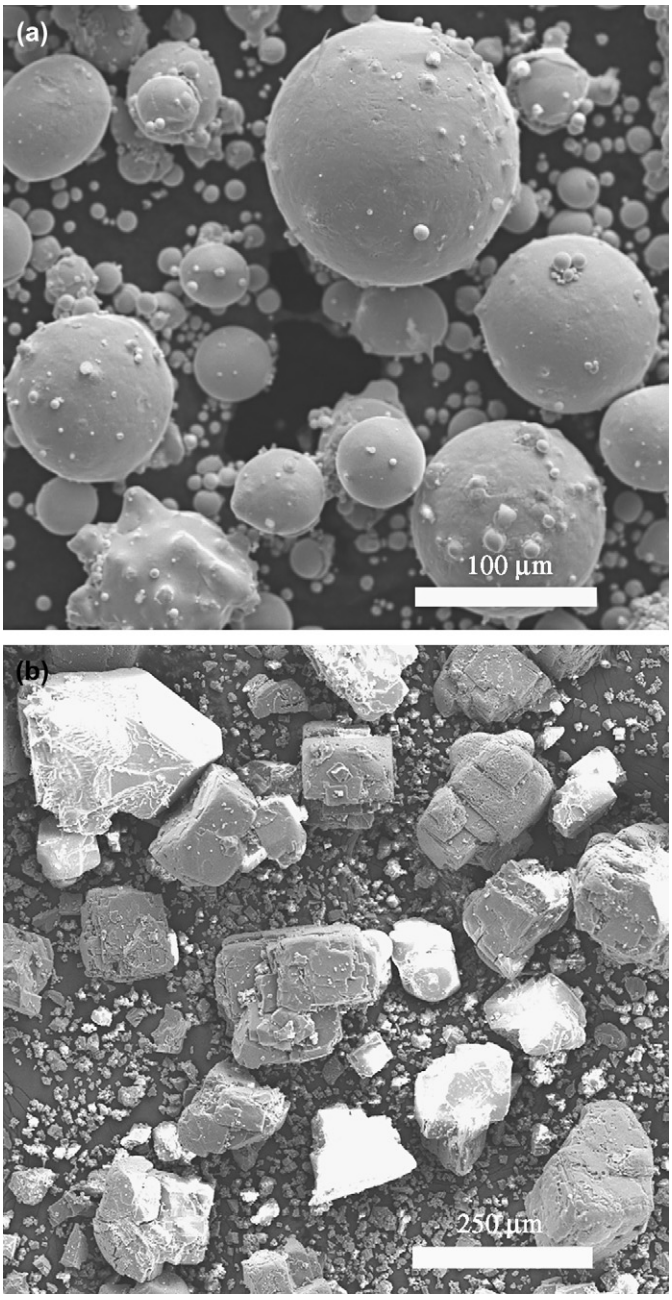

Fig. 1. SEM micrographs of initial powders: (a) NiTi, (b) NaF.

The consolidated NiTi–NaF composite billet was cut with a diamond saw at slow cutting rate to make samples with a dimension of $5 \times 10 \times 10\ mm^3$. The samples were then suspended in circulating water to dissolve the NaF phase. The sample mass was measured to track weight loss during dissolution. All salt was considered removed after 2 weeks, when the sample mass reached the expected value corresponding to volume fraction and bulk density of NiTi and did not change. After salt removal, samples were divided into two groups: a first group (labeled H for HIP) was characterized in the as-HIP condition while a second group (labeled HS

for HIP/sinter) was subjected to a subsequent sintering step under high vacuum (0.01 mtorr gage vacuum) at 1250 °C for 24 h, using a heating and cooling rate of 7 K min^{-1}. Titanium getters were used to minimize oxidation of the sample by residual gases.

2.2. Foam characterization

Cross-sections of billets H and HS were infiltrated with epoxy resin, polished to 0.5 μm grit and examined with a scanning electron microscope (SEM). SEM images were used to determine an average linear pore size by the line-intercept method as $1.12L_o/N_{pore}$ [39] where L_o is the line length and N_{pore} is the number of pores on that line. Closed and open porosities were calculated by helium pycnometry and Archimedes water displacement (after applying a thin coating of vacuum grease on the sample surface), using a NiTi density of 6.45 g/cm^3 [40]. Differential scanning calorimetry (DSC) was carried out on NiTi powders and small H and HS samples using a Perkin–Elmer DSC-7 apparatus at a rate of 10 K/min under nitrogen cover gas. Two temperature cycles were carried out between −60 (or in some cases 0 °C) and 170 °C and the second cycle was used to determine transformation temperatures (from the intersection between the baseline and the steepest slopes of the peak) and the transformation enthalpy (from integration of the peak).

After salt removal, samples H and HS were cut by electro-discharge machining into mechanical test samples with parallelepiped $4 \times 4 \times 8$ mm^3 shape. To remove the thin surface layer damaged during machining, the sample surfaces were lightly polished on grit paper. The samples were then annealed in an oil bath at 160 ± 2 °C for 5 min and oil-quenched to room temperature, to reduce any effect of the prior stress and thermal history.

The compression experiments were conducted at ambient temperature in a screw-driven load frame with engineering strain being determined from crosshead motion corrected by the previously-measured compliance of the system. Each sample was loaded and unloaded at a constant crosshead displacement rate of 0.05 mm/min between a minimum strain of 0% and a maximum strain ε_{max}, with ε_{max} increasing in 1% increments from 1 to 6% for foam H and from 1 to 8% for foam HS over six, respectively eight, consecutive loops. Average loading and unloading stiffness values, E_{load} and E_{unload}, were determined from the slope of a best linear fit of the loading curve and unloading curve, respectively, while ignoring the stress–strain data between 0 and 10 MPa (all compressive stresses and strains are reported as positive value in the present article), which were likely to be inaccurate due to sample settling effects. For unloading stiffness calculations, the data between the maximum stress σ_{max} and σ_{max} −10 MPa were also discarded, to avoid the steep stress drop at the beginning of unloading (assigned to machine mechanical hysteresis). The unloading strain was found from the change of length on unloading from maximum to zero stress, as measured by a micrometer with 1 μm accuracy. After its eighth cycle, foam HS was subjected to a final compressive loop to a maximum stress of 482 MPa and strain of 15.6%.

At the end of each of the mechanical loops, each sample was immersed in a 160 °C oil bath for 5 min and oil-quenched to room temperature (the same condition used in heat treating the samples before mechanical testing). This excursion above the austenite-finish (A_f) temperature leads to strain recovery, ε_{rec}, by the shape-memory effect, which was quantified by measuring the longitudinal dimension of the sample before and after the thermal recovery treatment with a micrometer with an accuracy of 1 μm. From the former measurement, the plastic strain after unloading, ε_{pl}, was also determined.

3. Results

3.1. Microstructure

Representative SEM micrographs of foams H and HS are shown in Figs. 2 and 3, respectively. Fig. 2(a) provides a view of the microstructure of foam H at low magnification, which illustrates that a porous structure was achieved after hot isostatic pressing and salt removal. The large pores (with size as large as 400 μm) correspond to the salt particles and have an irregular shape and average sizes of 242 ± 32 μm. The overall porosity of foam H is $39.5 \pm 0.1\%$ and its closed porosity is $2.8 \pm 0.6\%$; by subtraction, the open porosity is 36.7%. A higher magnification image of foam H (Fig. 2(b)) shows that individual NiTi powders are still identifiable but that they are connected with each other through sizeable necks. Closed porosity is probably associated with the small pores present between partially densified powders, with size typically under 10 μm. Incomplete sintering is also confirmed by the presence of individual NiTi powders lining the surface of the large pores, as shown in Fig. 2(c) for a sample not infiltrated with epoxy. No residual salt in the structure can be seen after dissolution. Moreover, neither reaction between NiTi and NaF (which may have occurred during HIP) nor corrosion of the NiTi (which may have occurred during salt dissolution) was observed.

SEM micrographs of foam HS (Fig. 3(a–c)) show the effect on the microstructure of the subsequent high-temperature sintering step. A significant increase in the overall degree of densification was observed, which was confirmed by density measurements showing a total porosity of $19.6 \pm 0.1\%$ which is half of the pre-sintering porosity. The closed porosity is $6.6 \pm 0.2\%$ more than twice the pre-sintering value. Accordingly, the open porosity (13.0%) is much reduced. Also, the pores were more rounded, their surfaces smoother, and their average size reduced to 177 ± 41 μm.

3.2. Phase transformation behavior

DSC thermograms of the NiTi powders and foams H and HS are shown in Fig. 4. Foam H exhibits phase transformations typical of bulk NiTi, with peaks resulting from the transformation between the low-temperature martensitic B19′ phase and the high-temperature austenitic B2 parent phase (and no second peak for the R-phase). To first order, the martensite start and finish (M_s and M_f), and the austenite start and finish (A_s and A_f) temperatures are given in Table 1, together

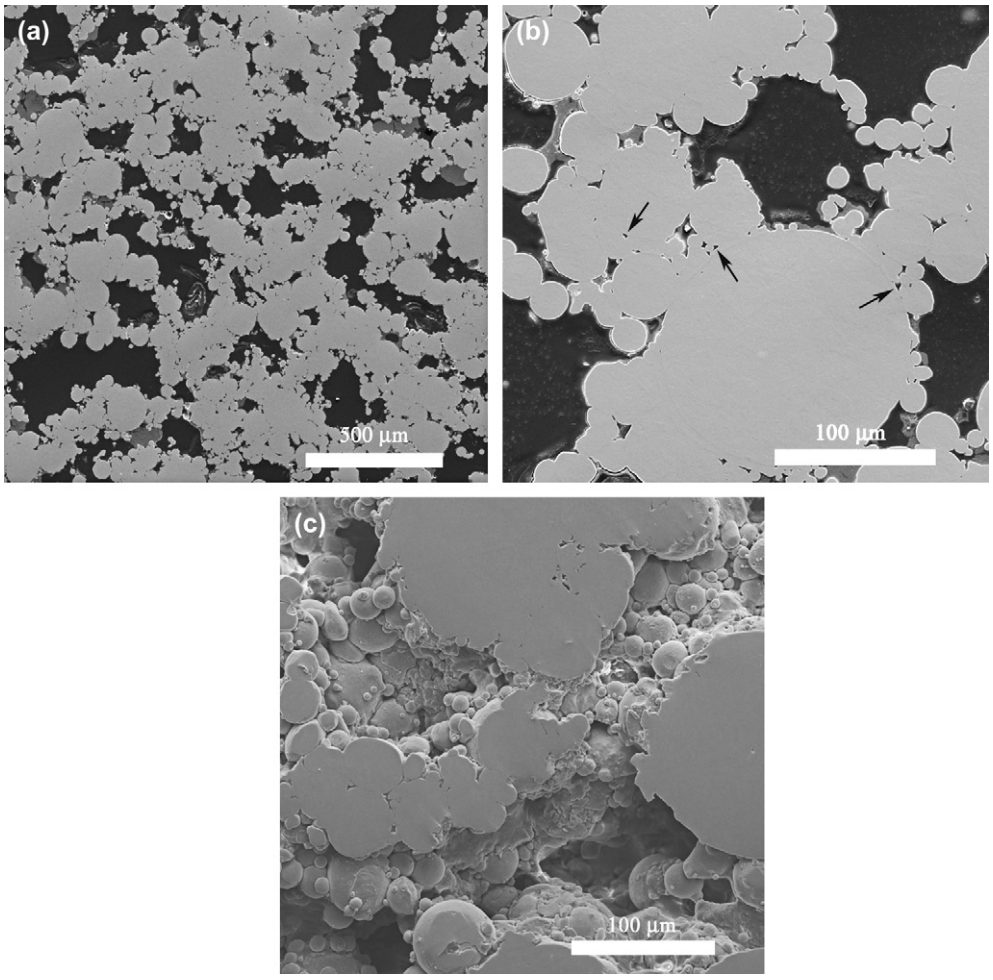

Fig. 2. SEM micrographs of 39.5% porosity foam H (densified by HIP and with salt removed): (a, b) resin-filled pores at low and high magnification, (c) unfilled pores.

with the transformation enthalpies calculated from the area of the transformation peaks. Given its M_f value of 55 °C, foam H is fully martensitic during mechanical testing at ambient temperature. Comparison between the NiTi powders and foam H (Fig. 4 and Table 1) shows that after HIP process the transformation enthalpies of NiTi remain nearly the same but the transformation temperatures is increased by about 10–30 °C.

As compared to foam H, foam HS shows a decrease in the transformation enthalpies (by about a factor 2), a decrease in transformation temperatures (by about 50 °C for M_f and A_f and 110 °C for M_s and A_s), and an increase in the spread between start and finish temperatures (Fig. 4 and Table 1). Given its M_s value of 24 °C, foam HS consists of metastable austenite at the onset of mechanical testing at ambient temperature.

3.3. Mechanical and shape-memory properties

Fig. 5(a and b) displays for foams H and HS the stress–strain curves from the series of compressive load–unload-recovery tests. Strain recovery by reverse transformation upon heating after each compressive load–unload loop is indicated by a horizontal arrow for each cycle. It is apparent from Fig. 5(a) that foam H exhibits near linear stress–strain curves, with plastic strain accumulated after each cycle increasing from 0.5 to 5%. Five load–unload-recovery cycles were carried out before the final cycle (maximum strain of 6% and maximum stress of 135 MPa) led to large-scale damage visible as a stress drop before unloading. In the first five cycles, the shape-memory recovery (expressed as a fraction of the plastic strain) is near constant at 85–89%, but decreases to 71% for the last cycle where damage had accumulated.

Foam HS (Fig. 5(b)) shows a load–unload-recovery behavior that is generally similar to foam H, but with some important differences, as expected from its lower porosity and lower transformation temperatures. For a given maximum strain, the stress is much higher, corresponding to a higher average stiffness on loading. On unloading, however, the strain recovery is higher than for foam H, corresponding to a lower unloading stiffness. Also, as compared to foam H, the magnitude of the shape-memory recovery of foam HS is much reduced, and somewhat reduced when normalized by the plastic strain accumulated after each load–unload cycle. Finally, the last cycle shown in Fig. 5(c) is characterized by a near linear range up to a stress of ~400 MPa and a strain of ~7%, followed by a plateau with a much lowered slope up to the highest stress of 482 MPa and a strain of 15.6%, terminated by the beginning

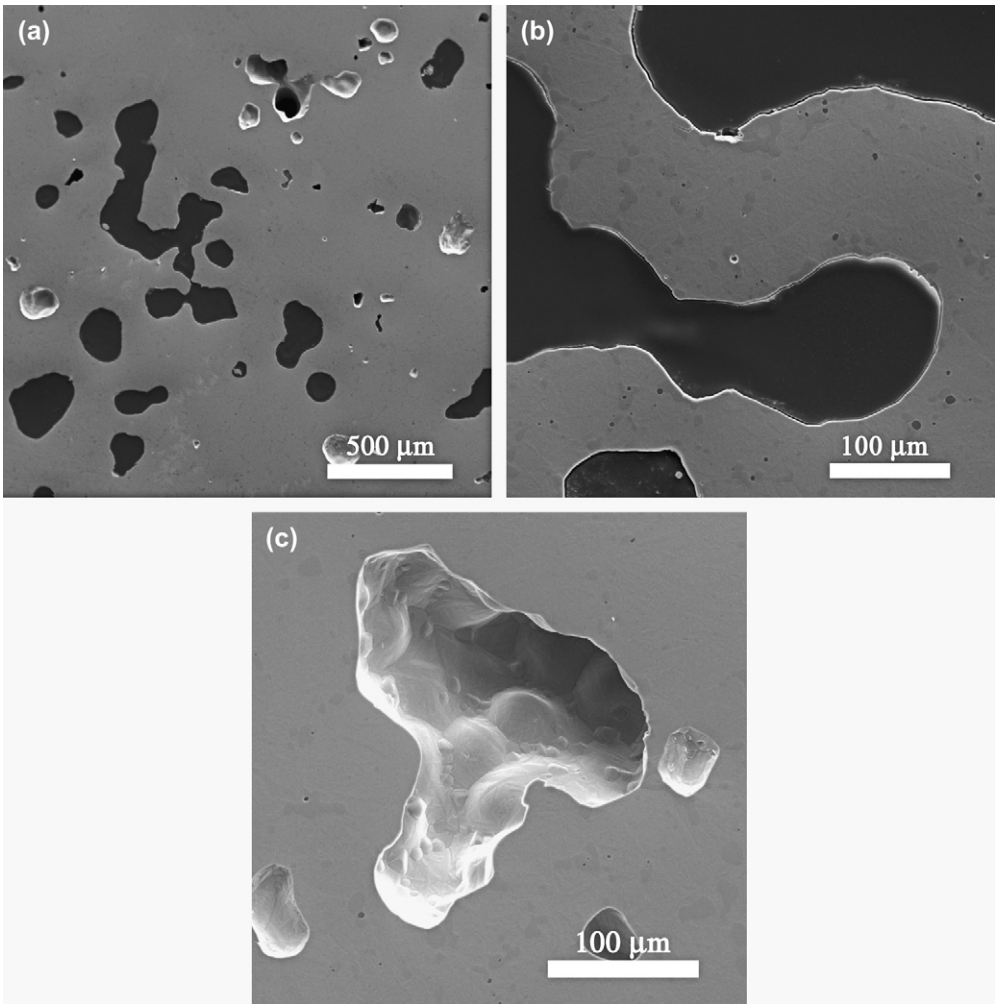

Fig. 3. SEM micrographs of 19.6% porosity foam HS (processed like foam H and additionally vacuum-sintered): (a, b) resin-filled pores at low and high magnification, (c) unfilled pores.

of stress drop. A much reduced, but still sizeable, shape-memory strain (2.7% or about a quarter of the residual strain after unloading) was measured.

Fig. 6(a and b) depicts the stress–strain curves for foams H and HS for a maximum strain of 5%. The method for evaluating strains and average stiffnesses are illustrated on each plot. It is apparent that stiffness values can vary noticeably from point to point as compared to the average value, indicating that the foams are not deforming in a purely elastic manner (we thus use the term average stiffness rather than Young's modulus). It is also noticeable from the unloading curve (in particular from the sharp strain recovery below 25 MPa) that foam HS shows superelastic strain recovery, which is followed by a sizeable shape-memory strain recovery during the thermal excursion.

4. Discussion

4.1. Microstructure

For foam H, open porosity (36.7%) represents the vast majority of the overall porosity (39.5%), as expected since the salt leaching process implies an open and connected pore network. The closed porosity (2.8%) is expected to be empty because no salt was observed during metallographic examination, and because the salt fraction is well above the percolation threshold. Thus, closed porosity is most probably due to the incomplete densification of the NiTi powders, illustrated in Fig. 2(b). Then, the small discrepancy between the open porosity (36.7%) and the NaF initial volume fraction (40.1%) is assigned to inhomogeneities during packing of the powder blend in the HIP can, explainable by the large mismatch in densities between NiTi (6.45 g/cm^3) [40] and NaF (2.78 g/cm^3) [41]. In fact, this large density mismatch is the reason why coarser NaF powders were not used, despite the improvement in powder packing (and thus eventual densification) provided by blends with powders of different sizes: it was not possible to uniformly mix coarser NaF (250–350 μm) with the present NiTi powders.

The size and shape of the large pores in foam H (Fig. 2(a)) are similar to those of the NaF powder (Fig. l(b)). Some of the largest pores may have been due to agglomeration of a few NaF powders. The irregular shape of the large pores also indicates that, during the HIP process, the NaF powders do not deform significantly. This suggests that pore shape and size can

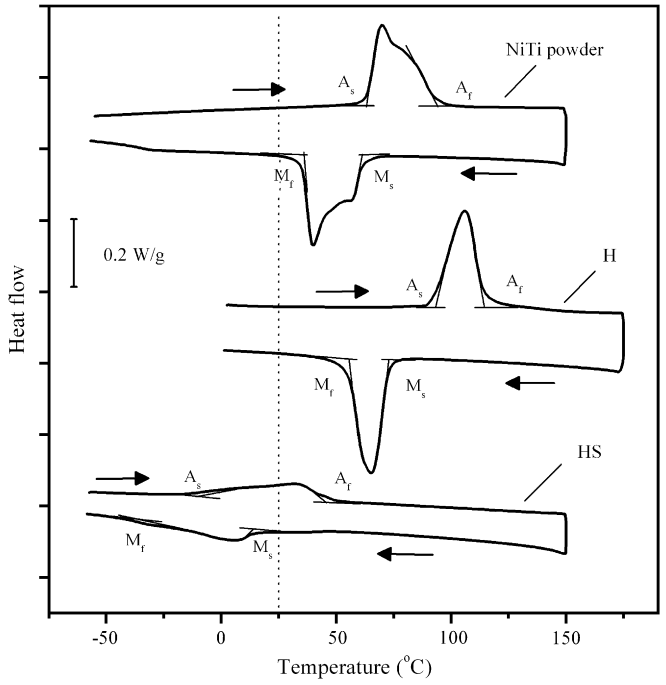

Fig. 4. DSC curves of NiTi powder and foams H and HS.

be controlled by the NaF space-holder, but not to the same extend as in replicated foams using liquid metal infiltration [42] since densification of the NiTi powders also determines the quality of the pore surface. As shown in Fig. 2(a–c), individual rounded NiTi powders are still visible, thus giving a rough topography to the inner surface of the larger pores.

Another consequence of the incomplete densification of the NiTi powders in foam H is the presence of finer pores present between NiTi powders (some of which are marked with arrows in Fig. 2(b)). The closed porosity of 2.8% is most probably associated with these small pores, which were probably never filled with NaF as discussed above. Optimization of the HIP parameters or further sintering after the HIP process may increase the densification of the NiTi powders and eliminate these fine pores. For the former option, higher HIP pressure and/or higher HIP temperature (using higher-melting salts such as BaF_2 or SrF_2 which have been used successfully for replication of Zr-based foams [43,44]) could be used.

Table 1
Transformation temperatures and enthalpy on heating and cooling for NiTi powder, foam H and foam HS

	Powder	Foam H	Foam HS
Heating			
A_s (°C)	63	92	−18
A_f (°C)	93	114	47
Enthalpy (J/g)	23.8	23.9	10.9
Cooling			
M_s (°C)	61	73	24
M_f (°C)	35	55	−45
Enthalpy (J/g)	23.8	24.0	11.3

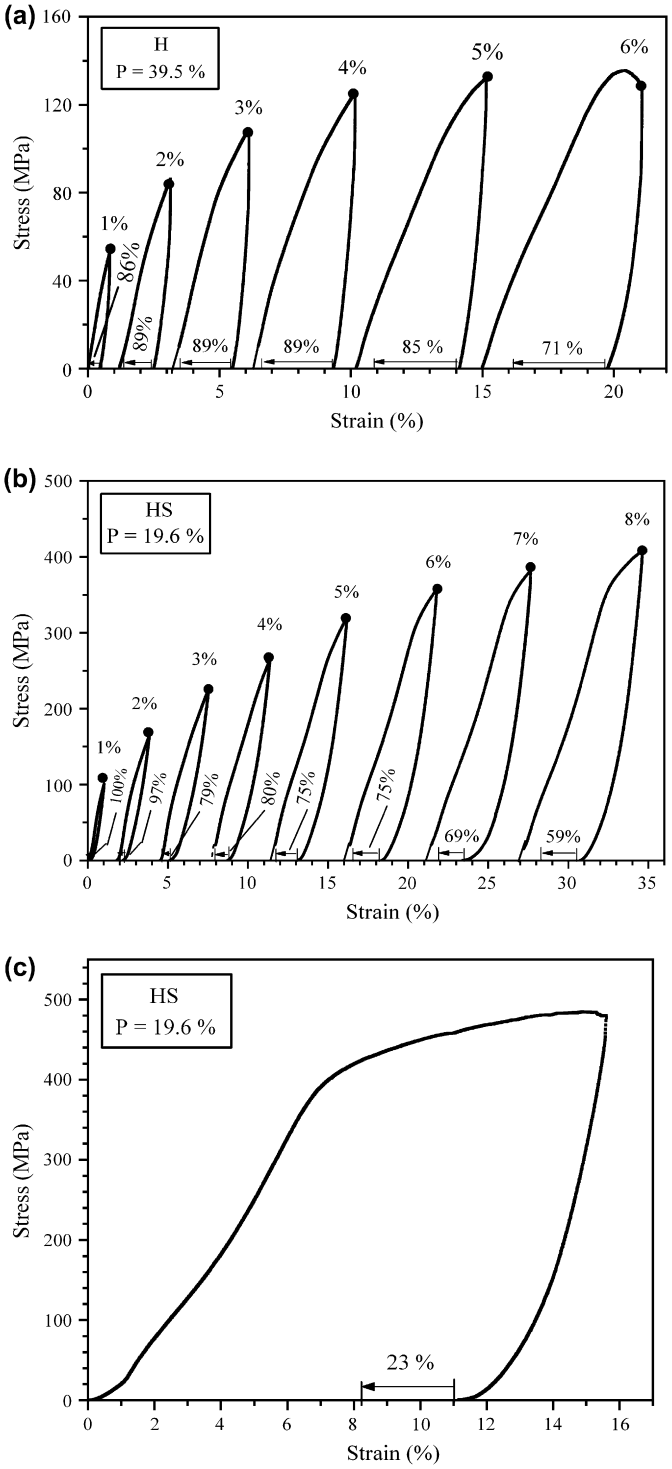

Fig. 5. Series of compressive stress–strain curves (load–unload) for increasing maximum strains for (a) foam H, (b) foam HS. Curves are shifted along the *y*-axis for clarity. Arrows along the *y*-axis for each curve represent the thermally-recovered shape-memory strain. The stress at which the sample is unloaded is marked with a dot. (c) Final compressive stress–strain curve for foam HS up to maximum strain of 15.6%.

In the present work, a high-temperature sintering step was chosen to further densify the NiTi powders, resulting in foam HS. This step reduced overall porosity by a factor two and altered significantly pore shape and size, as illustrated in

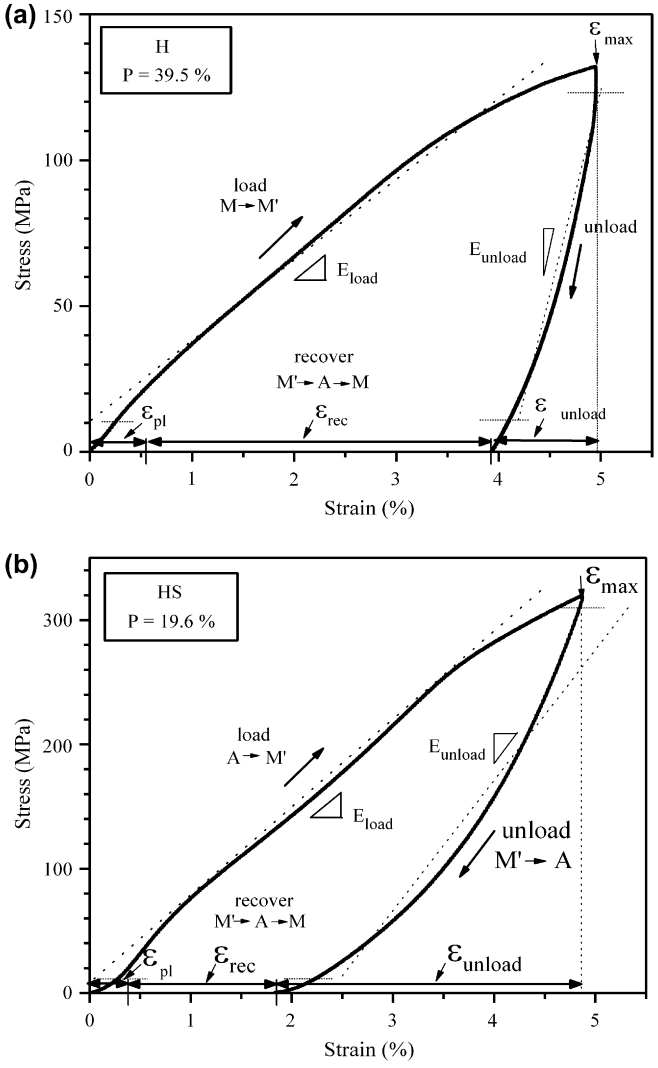

Fig. 6. Compressive stress–strain curves for a maximum strain of 5%: (a) foam H, (b) foam HS. Evaluation method for loading and unloading stiffnesses, and for the unloading, shape-memory and plastic strains are illustrated, together with the phases expected (A – austenite, M – martensite, M′ – detwinned martensite).

Fig. 3(a–c): the large pores previously occupied by NaF powders exhibit smaller sizes, more rounded shapes and much smoother inner surfaces than those in foam H. Individual NiTi powders are not visible anymore, unlike for foam H, and the fine cusped pores between NiTi powders have disappeared. The overall porosity is 19.6%, close to the percolation limit; accordingly, about one third of the porosity (6.6%) is now closed, while two thirds (13.0%) remain open. Foam HS thus represents an upper limit in foam densification, beyond which alternate processes might be better suited, e.g., pore expansion by entrapped gas, as done by Greiner et al. [28] who reported porosities of 19–20% after 100 to 200 h of expansion at 1200 °C. In that study, however, the NiTi porosity was fully closed. Sintering of foam H at lower temperature and/or shorter time is expected to produce foams with structure and porosities intermediate between those of foams H and HS.

4.2. Phase transformation behavior

The DSC thermogram in Fig. 4 indicates that foam H is fully martensitic during testing at ambient temperature after oil quenching from the annealing temperature of 160° C, and that the reverse transformation upon heating is complete well below the temperature of 160 °C used to induce the shape-memory effect. These transformation temperatures (Table 1) are typical of stoichiometric, or slightly nickel-poor, NiTi compositions [45]. The transformation enthalpies for foam H on both heating and cooling are very close to published values for bulk NiTi (24.3 J/g) [40]. This implies that neither the HIP process nor the salt dissolution step significantly affected the composition of foam H.

The transformation enthalpies for the NiTi powder are similar to those of foam H, indicative of full transformation. The significant lower transformation temperatures and presence of double peaks on both heating and cooling may be the result of internal stress in the powders, expected from their fabrication by rapid solidification (inferred from their spherical shape).

The shift in transformation temperature as well as the reduction in transformation enthalpy observed for foam HS (Fig. 4) is indicative of composition changes occurring during the 24 h vacuum-sintering treatment. It is likely that residual gases in the furnace were sufficient to oxidize (or nitride) preferentially titanium, resulting in a slightly Ni-rich composition: for Ni-content in excess of approximately 49.6 at.%, the M_s temperature drops precipitously by about 90 °C for each at.% Ni [45]. The broadening in the transformation peaks for foam HS may also reflect that some regions of the foam (probably near the surfaces where reaction with gas was more extensive) are more Ti-depleted than others (away from the surface), and the reduction in transformation enthalpy may indicate that parts of the sample (near the surface) do not transform at the lowest used temperature of −60 °C. After quenching to ambient temperature, foam HS is expected to consist completely of metastable austenite, given the M_s and A_s temperatures of 24 and −18 °C, thus affecting its mechanical properties, as described in the next section.

4.3. Mechanical behavior

4.3.1. Stiffness

Foam H with 39.5% porosity is characterized by near linear loading and unloading (Fig. 5(a)), except for the last loop where damage occurred. The foam is fully martensitic, so detwinning is expected to occur during loading. While no stress plateau is visible, the anomalously low value of the loading stiffness, which is plotted in Fig. 7 for all loops, is a strong indication that detwinning occurs continuously during the loading part of the stress–strain curve. This is confirmed by two further observations. First and most directly, a significant shape-memory effect is measured after thermal excursion, as indicated in Fig. 5(a). Second, the unloading stiffness, which is expected to be mostly elastic (assuming no reverse detwinning), is 3–4 times higher than the loading stiffness (Fig. 7), which must thus contain significant contribution from

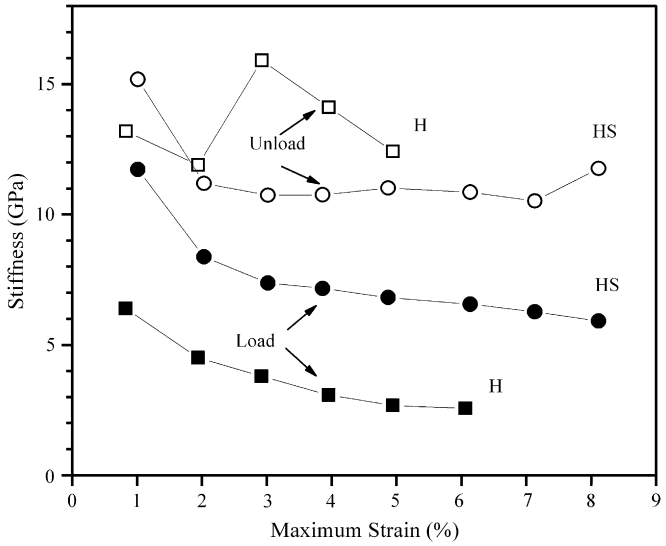

Fig. 7. Loading and unloading stiffness as a function of maximum compressive strain for foams H and HS.

detwinning. We note, however, that the unloading stiffnesses (12–16 GPa) are significantly lower than predicted from Ashby's theory for open cell, cellular foams, which is expected to be $(1-P)^2 E_{\mathrm{NiTi}} = 22$–$25$ GPa based on porosity $P = 0.395$ and Young's modulus $E_{\mathrm{NiTi}} = 61$–69 GPa [46]. This discrepancy on unloading may be due to some reverse detwinning or, more likely, to an inherently lower elastic stiffness due to deviation from the cellular architecture assumed for the above model, and the presence of non-load-bearing metal extrusions in the pores.

If foam H were mechanically cycled without intermediate shape-memory recovery, the loading stiffness would be expected to become similar to the measured unloading stiffness, i.e., 12–16 GPa, since detwinning on loading would be exhausted in the first cycle. This stiffness range is exceptionally low as compared to other metallic foams, a property that may be useful for bone-replacement implants whose stiffness should ideally match that of bone (12–17 GPa for compact bone [47]). It is difficult to compare the stiffness of foam H, which is martensitic, with that of other published NiTi foams, which are all austenitic and can thus show extraordinary low stiffness due to the superelastic effect. For example, an open-cell austenitic NiTi foam with the same range of porosity (42%) and pore size (500 μm) as foam H, but produced by SHS followed by gas expansion [6], has a similar stiffness (15 GPa) at 60°C (above A_f) as that measured here for foam H.

Given that foam HS has much lower porosity than foam H and consists of metastable austenite, it is not surprising that its loading and unloading stiffnesses are quite different from those of foam H. The lower porosity increases its Young's modulus, but its austenitic structure allows for the activation of superelastic deformation on both loading and unloading thus reducing its average stiffness. As shown in Fig. 7, the interplay between these different mechanisms (elastic and detwinning deformation for foam H and elastic and superelastic deformation for foam HS) leads to the unusual situation where stiffness for foam HS is higher on loading but lower on unloading than for foam H. Thus, on loading, martensite detwinning in foam H produces larger strain (and thus lower stiffness) than stress-induced formation of martensite in foam HS. However, on unloading, foam H does not show significant reverse detwinning, while foam HS recovers strain superelastically by reverse martensite–austenite transformation. As a result, load and unload stiffnesses are in a relatively narrow range of 6–12 GPa for foam HS. For comparison, an austenitic sample with 16 vol.% of closed porosity produced by gas expansion showed an average loading stiffness (from 0 to 400 MPa, similar to the last loop of foam HS) of about 15 GPa [28].

4.3.2. Strength

The ultimate compressive stress of 135 MPa obtained from foam H with 39.5% porosity (Fig. 5(a)) is low as compared with porous NiTi with the same level of porosity produced by different methods: 245 MPa for austenitic NiTi with 42% open porosity produced by gas expansion [6], 180 MPa for austenitic NiTi with 30–40% open porosity produced by sintering of elemental powders [48], 275 MPa for austenitic NiTi with 27% partially open porosity produced by capsule-free HIP [13]. Direct comparison is again complicated by the different phases present (and thus the inherent strength of the NiTi material present in the foam), and the fact that foam H had been subjected to five prior stress–strain-recovery cycles which may have produced damage. It is, however, likely that the highly irregular pore shape (acting as internal notches) contributes to the relatively low strength observed in foam H.

Foam HS showed a marked improvement in ultimate strength (which is in excess of 482 MPa, Fig. 5(c)), as expected from the reduced level of porosity, the more equiaxed pore shape and the smoother pore surface. For comparison, an austenitic foam with 16% closed porosity displayed no fracture up to a stress of close to 1000 MPa [28].

4.3.3. Shape-memory strain recovery

Fig. 8(a) presents for foam H unloading strain, shape-memory recovery strain and residual plastic strain (these strains are illustrated in Fig. 6(a) and are determined from the six load–unload-recovery curves in Fig. 5(a)). It is apparent that the shape-memory strain increases near linearly with the maximum applied strain, up to a maximum value of 3.2%. In bulk NiTi too, the shape-memory strain increases near linearly with the applied strain, a behavior associated with the stress plateau during which detwinning takes place [38]. Such a constant-stress plateau is, however, not visible in foam H, or rather the whole loading branch of the stress–strain curve can be considered as a steadily increasing plateau where twinning occurs continuously.

The compressive shape-memory recovery capability of foam H is similar to that for pore-free NiTi produced from the same pre-alloyed powders [38]. For a residual strain after unloading of ~2% (accumulated at the end of the 3% load–unload cycle in Fig. 5(a)), foam H recovers 89% of this strain, while pore-free NiTi recovers 87% [49]. For a residual strain

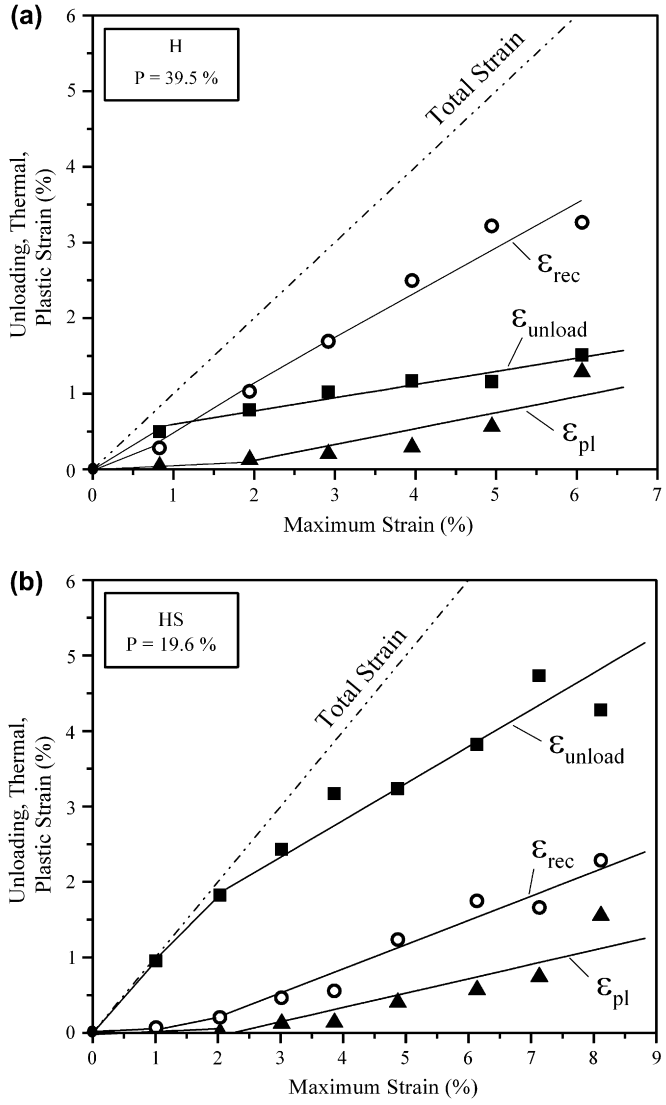

Fig. 8. Unloading, shape-memory and plastic strain as a function of maximum compressive strain for: (a) foam H; (b) foam HS.

of ∼4% (4.4% for bulk NiTi and 3.9% for foam H after the 5% cycle in Fig. 5(a)), the shape-memory recovery is again very similar (83% for bulk NiTi and 85% for foam H). The maximum stresses to achieve those strains are, however, much higher for bulk NiTi (∼370 MPa for 2% residual strain, and ∼910 MPa for 4.4% [49]) than for foam H (108 and 131 MPa, respectively). Thus, at least for the relatively low shape-memory strains studied here (<3.2%), the foam strain recovery is similar to bulk NiTi, but necessitates much lower stresses for a given deformation level.

The maximum shape-memory recovery strain (3.2% for the 5% and 6% cycles, Figs. 5(a) and 8(a)) are, however, lower than the maximum value of 4.5% recoverable in compression for bulk NiTi (albeit after deformation to a much higher stress of ∼1300 MPa) [49]. A likely reason is the early onset of dislocation plasticity and damage in foam H at regions of stress concentrations, which inhibit the shape-memory recovery. Improvements in the foam architecture would likely increase the maximum recoverable shape-memory strain in foamed NiTi.

Also noteworthy for foam H is the large unloading strain of 1.5% for the maximum strain of 6%. For comparison, pore-free NiTi has about the same unloading strain of 1.6% for the same maximum strain of 6% [49], but at a much higher maximum stress of ∼900 MPa. As discussed earlier, this large unloading strain in foam H is the result of the anomalously low value of its unloading stiffness, which may be associated with some reverse twinning and/or large elastic deflections due to uneven pore geometries. Thus, foam H, when compressed to a relatively modest (as compared to bulk NiTi) stress of 135 MPa, is capable of recovering a total strain of 4.8% by combination of unloading and shape-memory strains, with a relatively low plastic, unrecoverable strain of 1.3%.

4.3.4. Superelastic strain recovery

Fig. 8(b) shows that recovery in foam HS is dominated by the unloading strain through a combination of elastic and superelastic effects. A sizeable shape-memory strain is furthermore achieved during the thermal excursion. The coexistence of both superelastic and shape-memory effects can be explained as follows. Before loading, the sample is fully austenitic, but very close to forming martensite (given its M_s temperature of 24 °C). On loading, stress-induced martensite is formed, and a fraction of this martensite disappears on unloading, producing the superelastic strain. But another fraction of the martensite remains in the sample after full unloading, given that the A_f temperature of 47 °C is well above room temperature. Only upon subsequent heating to 160 °C does this martensite disappear, producing the shape-memory strain.

For an applied strain of 7% at a stress of 380 MPa, a maximum unloading (elastic and superelastic) strain of 4.7% is achieved, which is compounded by a subsequent shape-memory recovery stain of 1.7%, for a total recoverable strain of 6.4%. A similar total recovered strain of 6.6% is achieved for the 8% cycle (with a maximum stress of 406 MPa), with slightly less unloading strain and slightly more recovery strain (Fig. 8(b)). For comparison, an austenitic NiTi foam with 16% closed porosity exhibited an unloading strain less than 2.5% for a similar maximum stress of 400 MPa [28]. However, foam HS was not heat-treated to develop optimal superelastic properties, so comparisons with other literature results on superelastic NiTi foams are not attempted.

5. Conclusions

Open porosity NiTi foams with shape-memory properties were fabricated by a solid-state replication method, where a mixture of pre-alloyed NiTi and NaF powders is densified by hot isostatic pressing at 950 °C into a billet from which the NaF space-holder is subsequently removed by water dissolution. The resulting martensitic NiTi foam, with a mostly-open porosity of 39.5%, exhibits pores with a ragged internal surface due to incomplete sintering of NiTi powder particles. The following mechanical properties in compression are measured: (i) a near linear loading stress–strain curve, with a very low average stiffness of 3–6 GPa, as a result of detwinning on loading; (ii) a near linear unloading stress–strain curve, with

an average stiffness of 12–16 GPa indicative of elastic deformation; (iii) an ultimate compressive strength of 127 MPa at 6% strain; (iv) a large shape-memory recovery, with 85–89% of the strain accumulated on unloading recovered after a thermal excursion, and a maximal value of 3.2%.

After sintering at 1250 °C, the foam showed a reduced porosity of 19.6% (a third of which was closed), smaller and smoother pores, and a shift in transformation temperature most probably due to oxidation. This metastable austenitic foam exhibits the following mechanical properties: (i) near linear loading and unloading stress–strain curves, with average stiffness of 6–12 GPa, as a result of the superelastic effect; (ii) much higher ultimate strength (>482 MPa) and strain (>15.6%); (iii) a sizeable shape-memory-recovery, which, when added to the elastic and superelastic recovery strain on unloading provides a total recovery strain of up to 6.5%.

Acknowledgments

This research was supported by the U.S. National Science Foundation (Grant DMR-0505772). A.B. gratefully acknowledges the support, through the Royal Thai Government Scholarship, of the Ministry of Science (Thailand). Useful discussions with Mr. S.M. Oppenheimer (Northwestern University) are also acknowledged.

References

[1] Otsuka K, Wayman CM. , Shape memory materials. Cambridge, New York: Cambridge University Press; 1998.
[2] Kang SB, Yoon KS, Kim JS, Nam TH, Gjunter VE. In vivo result of porous TiNi shape memory alloy: bone response and growth. Mater Trans 2002;43:1045–8.
[3] Rhalmi S, Odin M, Assad M, Tabrizian M, Rivard CH, Yahia LH. Hard, soft tissue and in vitro cell response to porous nickel–titanium: a biocompatibility evaluation. Biomed Mater Eng 1999;9:151–62.
[4] Ayers RA, Simske SJ, Bateman TA, Petkus A, Sachdeva RLC, Gyunter VE. Effect of nitinol implant porosity on cranial bone ingrowth and apposition after 6 weeks. J Biomed Mater Res 1999;45:42–7.
[5] Simske SJ, Ayers RA, Bateman TA. Porous materials for bone engineering. Mater Sci Forum 1997;250:151–82.
[6] Lagoudas DC, Vandygriff EL. Processing and characterization of NiTi porous SMA by elevated pressure sintering. J Intell Mater Syst Struct 2002;13:837–50.
[7] Zhao Y, Taya M, Izui H. Study on energy absorbing composite structure made of concentric NiTi spring and porous NiTi. Int J Solids Struct 2006;43:2497–512.
[8] Qidwai MA, DeGiorgi VG. Numerical assessment of the dynamic behavior of hybrid shape memory alloy composite. Smart Mater Struct 2004;13:134–45.
[9] Zhou JB, Gao LP, Wang KS. Preparation of Ti–Ni porous alloys and its hydrogen isotope effects. J Rare Earths 2005;23:449–51.
[10] Elzey DM, Sofia AYN, Wadley HNG. A shape memory-based multifunctional structural actuator panel. Int J Solids Struct 2005;42:1943–55.
[11] Sugiyama M, Hyun S-K, Tane M, Nakajima H. Fabrication of lotus-type porous NiTi shape memory alloys. Porous metals and metal foaming technology, MetFoam 2005. The Japan Institute of Metals 2006;233–6.
[12] Grummon DS, Shaw JA, Gremillet A. Low-density open-cell foams in the NiTi system. Appl Phys Lett 2003;82:2727–9.
[13] Yuan B, Zhang XP, Chung CY, Zeng MQ, Zhu M. A comparative study of the porous TiNi shape-memory alloys fabricated by three different processes. Metall Mater Trans A 2006;37A:755–61.
[14] Bertheville B. Porous single-phase NiTi processed under Ca reducing vapor for use as a bone graft substitute. Biomaterials 2006;27:1246–50.
[15] Sakurai N, Takekawa J. Shape recovery characteristics of NiTi foams fabricated by a vacuum process applied to a slurry. Mater Trans 2006; 47:558–63.
[16] Wu SL, Chu PK, Liu XM, Chung CY, Ho JPY, Chu CL, et al. Surface characteristics, mechanical properties, and cytocompatibility of oxygen plasma-implanted porous nickel titanium shapememory alloy. J Biomed Mater Res A 2006;79A:139–46.
[17] Sadrnezhaad SK, Arami H, Keivan H, Khalifezadeh R. Powder metallurgical fabrication and characterization of nanostructured porous NiTi shape-memory alloy. Mater Manuf Processes 2006;21:727–35.
[18] Panigrahi BB, Godkhindi MM. Dilatometric sintering study of Ti-50 Ni elemental powders. Intermetallics 2006;14:130–5.
[19] Zhu SL, Yang XJ, Fu DH, Zhang LY, Li CY, Cui ZD. Stress–strain behavior of porous NiTi alloys prepared by powders sintering. Mater Sci Eng A 2005;408:264–8.
[20] Zhao Y, Taya M, Kang YS, Kawasaki A. Compression behavior of porous NiTi shape memory alloy. Acta Mater 2005;53:337–43.
[21] Li Q, Yu JY, Mu BC, Sun XD. BP neural network prediction of the mechanical properties of porous NiTi shape memory alloy prepared by thermal explosion reaction. Mater Sci Eng A 2006;419:214–7.
[22] Biswas A. Porous NiTi by thermal explosion mode of SHS: processing, mechanism and generation of single phase microstructure. Acta Mater 2005;53:1415–25.
[23] Chu CL, Chung CY, Lin PH, Wang SD. Fabrication and properties of porous NiTi shape memory alloys for heavy load-bearing medical applications. J Mater Process Technol 2005;169:103–7.
[24] Prymak O, Bogdanski D, Koller M, Esenwein SA, Muhr G, Beckmann F, et al. Morphological characterization and in vitro biocompatibility of a porous nickel–titanium alloy. Biomaterials 2005;26:5801–7.
[25] Yeh CL, Sung WY. Synthesis of NiTi intermetallics by self-propagating combustion. J Alloys Compd 2004;376:79–88.
[26] Kim JS, Kang JH, Kang SB, Yoon KS, Kwon YS. Porous TiNi biomaterial by self-propagating high-temperature synthesis. Adv Eng Mater 2004;6:403–6.
[27] Li BY, Rong LJ, Li YY, Gjunter VE. Fabrication of cellular NiTi intermetallic compounds. J Mater Res 2000;15:10–3.
[28] Greiner C, Oppenheimer SM, Dunand DC. High strength, low stiffness, porous NiTi with superelastic properties. Acta Biomater 2005;1:705–16.
[29] Hakamada M, Kuromura T, Chen YQ, Kusuda H, Mabuchi M. Sound absorption characteristics of porous aluminum fabricated by spacer method. J Appl Phys 2006;100.
[30] Jiang B, Zhao NQ, Shi CS, Du XW, Li JJ, Man HC. A novel methodfor making open cell aluminum foams by powder sintering process. Mater Lett 2005;59:3333–6.
[31] Bram M, Stiller C, Buchkremer HP, Stover D, Baur H. High-porosity titanium, stainless steel, and superalloy parts. Adv Eng Mater 2000;2:196–9.
[32] Zhang EL, Wang B. On the compressive behaviour of sintered porous coppers with low to medium porosities – Part I: Experimental study. Int J Mech Sci 2005;47:744–56.
[33] Zhao YY, Fung T, Zhang LP, Zhang FL. Lost carbonate sintering process for manufacturing metal foams. Scripta Mater 2005;52:295–8.
[34] Li M, Liu Y, Ye JW, Zhang LF, Li J, Tu MJ. Process and compressive properties of porous nickel materials. Powder Metall 2006;49:114–7.
[35] Laptev A, Bram M, Buchkremer HP, Stover D. Study of production route for titanium parts combining very high porosity and complex shape. Powder Metall 2004;47:85–92.
[36] Esen Z, Bora S. Processing of titanium foams using magnesium spacer particles. Scripta Mater 2007;56:341–4.
[37] Patnaik P. Handbook of inorganic chemicals. New York: McGraw-Hill; 2003.
[38] Mari D, Dunand DC. Niti and Niti–Tic composites. I: Transformation and thermal cycling behavior. Metall Mater Trans A 1995;26:2833–47.
[39] Annual book of ASTM standards: metals test methods and analytical procedures. In: Metals – mechanical testing; elevated and low-temperature tests; Metallography. Philadelphia: ASTM; 2004. 267–292.
[40] Jackson CM, Wagner HJ, Wasilewski RJ. 55-Nitinol – The alloy with a memory: its physical metallurgy, properties, and applications, vol. 42.

Washington, D.C: National Aeronautics and Space Administration; 1972, Report no. NASA - SP 5110.
[41] Perry DL, Phillips SL. Handbook of inorganic compounds. Boca Raton,CRC Press; 1995.
[42] Gaillard C, Despois U, Mortensen A. Processing of NaCl powders of controlled size and shape for the microstructural tailoring of aluminium foams. Mater Sci Eng A 2004;374:250–62.
[43] Brothers AH, Scheunemann R, DeFouw JD, Dunand DC. Processing and structure of open-celled amorphous metal foams. Scripta Mater 2005;52:335–9.
[44] Brothers AH, Prine DW, Dunand DC. Acoustic emissions analysis of damage in amorphous and crystalline metal foams. Intermetallics 2006;14:857–65.
[45] Tosho S. In: Funakubo H, editor. Shape memory alloys. Precision machinery and robotics, vol. 1. Gordon and Breach Science Publishers; 1984.
[46] Dunand DC, Mari D, Bourke MAM, Roberts JA. NiTi and NiTi–TiC composites IV: neutron diffraction study of twinning and shape-memory recovery. Metall Mater Trans A 1996;27:2820–36.
[47] Gibson LJ, Ashby MF. Cellular solids. Cambridge: Cambridge University Press; 1997.
[48] Li BY, Rong LJ, Li YY. , Stress–strain behavior of porous Ni–Ti shape memory intermetallics synthesized from powder sintering. Intermetallics 2000;8:643–6.
[49] Fukami-Ushiro KL, Dunand DC. NiTi and NiTi–TiC composites. III: Shape-memory recovery. Metall Mater Trans A 1996;27:193–203.